



HAL
open science

Magnetism for understanding catalyst analysis of purified carbon nanotubes

Christine Bellouard, Guillaume Mercier, Sébastien Cahen, Jaafar Ghanbaja, Ghouti Medjandi, Jérôme Gleize, Gianrico Lamura, Claire Herold, Brigitte Vigolo

► **To cite this version:**

Christine Bellouard, Guillaume Mercier, Sébastien Cahen, Jaafar Ghanbaja, Ghouti Medjandi, et al.. Magnetism for understanding catalyst analysis of purified carbon nanotubes. Journal of Magnetism and Magnetic Materials, 2016, 411, pp.39-48. 10.1016/j.jmmm.2016.03.056 . hal-01513805

HAL Id: hal-01513805

<https://hal.univ-lorraine.fr/hal-01513805>

Submitted on 31 Aug 2023

HAL is a multi-disciplinary open access archive for the deposit and dissemination of scientific research documents, whether they are published or not. The documents may come from teaching and research institutions in France or abroad, or from public or private research centers.

L'archive ouverte pluridisciplinaire **HAL**, est destinée au dépôt et à la diffusion de documents scientifiques de niveau recherche, publiés ou non, émanant des établissements d'enseignement et de recherche français ou étrangers, des laboratoires publics ou privés.



Distributed under a Creative Commons Attribution - NonCommercial - NoDerivatives 4.0 International License

Magnetism for understanding catalyst analysis of purified carbon nanotubes.

Christine Bellouard¹, Guillaume Mercier¹, Sébastien Cahen¹, Jaafar Ghanbaja¹, Ghouti Medjahdi¹, Jérôme Gleize², Gianrico Lamura³, Claire Hérold¹, Brigitte Vigolo^{1,*}

¹Institut Jean Lamour, CNRS-Université de Lorraine, BP 70239, 54506 Vandœuvre-lès-Nancy, France

²Laboratoire de Chimie Physique-Approche Multi-échelle de Milieux Complexes-Université de Lorraine, 1 Bd Arago, 57078 Metz, France

³CNR-SPIN – Dipartimento di Fisica, via Dodecaneso 33, 16146 Genova, Italy

* Corresponding author. Tel: +33 383684646; fax: +33 383684615
E-mail: Brigitte.Vigolo@univ-lorraine.fr (Brigitte Vigolo)

Abstract. The precise quantification of catalyst residues in purified carbon nanotubes is often a major issue in view of any fundamental and/or applicative studies. More importantly, since the best CNTs are successfully grown with magnetic catalysts, their quantification becomes strictly necessary to better understand intrinsic properties of CNT. For these reasons, we have deeply analyzed the catalyst content remained in nickel-yttrium arc-discharge single walled carbon nanotubes purified by both a chlorine-gas phase and a standard acid-based treatment. The study focuses on Ni analysis which has been investigated by transmission electron microscopy, X-ray diffraction, thermogravimetry analysis, and magnetic measurements. In the case of the acid-based treatment, all quantifications result in a decrease of the nanocrystallized Ni by a factor of two. In the case of the halogen gas treatment, analysis and quantification of Ni content is less straightforward: a huge difference appears between X-ray diffraction and thermogravimetry results. Thanks to magnetic measurements, this disagreement is explained by the presence of Ni^{2+} ions, belonging to NiCl_2 formed during the Cl-based purification process. In particular, NiCl_2 compound appears under different magnetic/crystalline phases: paramagnetic or diamagnetic, or well intercalated in between carbon sheets with an ordered magnetic phase at low temperature.

Keywords. Superparamagnetism; spincrossover; carbon nanotubes; purification; magnetization; gas phase treatment

Highlights:

Cl-gas treatment of Ni catalyst of carbon nanotubes leads to NiCl_2 residue.

Magnetic measurements show the transformation of Ni^0 in Ni^{2+} through a purification process.

High temperature Cl treatment removes 75% of metallic impurities.

Cl-purification yields to an amount of metal of 1.5% in arc-discharge CNT samples.

1. Introduction

Carbon nanotubes (CNTs) and especially single walled carbon nanotubes (SWNTs) have remarkable intrinsic physical and chemical properties that make them as excellent candidates for fundamental studies and applications in many fields [1,2]. However, whatever the synthesis methods, as-produced CNT samples contain both secondary carbon products and metallic-based impurities involved in the growth mechanism as catalyst. They are often used in high content (10-30 wt.%) in order to improve the nanotube formation and limit that of carbon byproducts. These metal-based impurities are reported to dramatically modify both chemical and physical properties of CNT [3-7]. Without any post-synthesis purification treatment, SWNTs become unusable because their intrinsic properties are lost or hidden due to the presence of these metallic particles. For this very reason, the development of purification treatments is a long-standing and active research area. Standard processes are often multi-step and generally combine (i) a reflux in concentrated nitric acid solution in order to weaken the carbon shells and oxidize the metal-based impurities (ii) a gas-phase or wet oxidation and (iii) a final annealing treatment to restore the defects created through previous steps [8-16]. More recently, high temperature treatment under halogens were evidenced as an interesting alternative technique to selectively remove metal-based impurities [17,18]. The assessment of the efficiency of such treatment indeed depends on the reliability of quantitative analysis of the remaining impurities. On one hand, local or surface analysis such as X-ray photoelectron spectroscopy or transmission electron microscopy (TEM) are used to determine their size and/or their chemical nature, however they are inefficient for a quantitative analysis [19]. On the other hand, macroscopic techniques such as thermogravimetry analysis (TGA) provide a quantitative analysis but without any discrimination regarding the chemical nature of the impurities in the purified samples. Among them, magnetic analysis (MAG) is a less commonly used technique [20-22]. It has been however shown to be very helpful to quantify

magnetic residues from CNT samples [23,25]; especially because it is an ultrasensitive and non destructive method which can even detect very low amount of isolated paramagnetic impurities [19].

In this work, we have applied a Cl-based purification treatment on arc-discharged as-produced SWNTs under different temperature conditions. For comparison, a more standard purification method, based on an acid treatment has also been applied. Analysis and quantification of Ni-based impurities have been investigated by TEM, X-rays diffraction (XRD), TGA and MAG. A good agreement between TGA and MAG is found for the acid treatment whereas a strong deviation is observed between the results obtained from the different used techniques in the case of the Cl-based treatment. Thanks to magnetic measurements, these discrepancies are attributed to oxidation of Ni⁰ into Ni²⁺ by the halogen gas. This result proves that chemical treatment used for purification can modify the impurity.

2. Experimental section

2.1. Sample preparation

The SWNTs used in this study have been synthesized in an arc-discharge homemade reactor described elsewhere [16]. The catalyst mixture is prepared with a graphite powder SFG6 (synthesized flake graphite 6 μ m) from Timcal, nickel particles of around 3 μ m purchased from Sigma Aldrich and yttrium powder (40 mesh) from Acros Organics. Ni/Y/C is fixed at 4.2/1/94.8 at.% (2.8/1/96.2 wt.%). The as-produced SWNT powder (referred as “raw”) was purified using 2 different treatments: (i) a standard purification process that involves an oxidation under dry-air at 350°C for 90 min, and a HCl (6N) reflux for 24 hours followed by an annealing treatment under high vacuum (around 10⁻⁶ mbar) at 1100°C for 60 min. The corresponding purified SWNT sample is referred as “sp”. (ii) Heating under chlorine partial pressure of 0.9 atm (90 % vol. of Cl₂ and 10 % vol. of N₂, total pressure being 1 atm) for 2 hours at 800°C, 950°C, or 1100°C; and a washing with hydrochloric acid (4 N) is also performed at room temperature overnight to solubilize the possible remaining metal chloride formed during the reaction with chlorine.¹⁷ After filtration, washing with pure water and drying, the purified SWNT samples at 800°C, 950°C, 1100°C were assigned to “hp-800”, “hp-950”, “hp-1100”, respectively.

2.2. Characterization Techniques

TEM observations were carried out using a Philips CM20 apparatus at an operating voltage of 200 kV. To increase the image contrast, holey carbon grids (200 mesh size) were used. A small amount of the powder is dispersed in ethanol using a low power sonication bath and deposited on the TEM grid. Around 30 images were analyzed for each sample with different magnifications and only representative images are shown. The mean size of the particles is determined from the size of at least 50 particles (and even more than 100 particles for the raw

sample). For hp-1100, the very low number of remaining particles has forbidden such measurement based on TEM.

XRD measurements were performed using a X'Pert PRO MPD (Multi Purpose Diffractometer) system with a copper (CuK_α) radiation ($\lambda = 1.54056 \text{ \AA}$) and a multiple strip X-Ray detector, X'celerator. The powder was placed on a silicon zero-background sample holder with a hole of a 1 mm-depth. For each sample, the hole is filled with the powder in the same manner keeping relatively constant the analyzed volume. Diffraction data were collected between 15° and 90° (2θ). For quantitative analysis (relative content and particle size), TOPAS (Total Pattern Analysis Solution) program based on a Rietveld analysis was performed on the Ni(200) peak.

Quantitative measurements of the metal-based particle content in the nanotube samples were obtained from the residue weight after TGA using a Setaram Setsys evolution 1750 Thermal Gravimetric Analyzer. The temperature is raised up to 1000°C under dry air at $3^\circ\text{C}/\text{min}$. Under these conditions, carbonaceous species are burnt off and the remaining metal-based particles are NiO and Y_2O_3 (checked by XRD, not shown). For our analysis, the remaining weight at typically 900°C is determined from at least three thermograms on the same sample, each recorded with about 5-10 mg of SWNT powder, in order to ensure reproducibility of the results.

Magnetic measurements have been performed with about 20 -30 mg of SWNT powder placed in a capsule closed with adhesive kapton using a squid-vibrating sample magnetometer (SVSM model from Quantum Design). The field dependence of the magnetization has been corrected from diamagnetic contribution of the sample and the sample holder by subtraction of the negative linear slope measured at 400K for $H > 40 \text{ kOe}$. Zero field cooled (ZFC) and field cooled (FC) magnetization have been measured from 3K to 400K at a rate of $+2\text{K}/\text{min}$

after a cooling at 12K/min. Magnetic isotherms have been measured in the same conditions for all samples: from 3K to 400K, after a cooling at 12K/min from 400K to 3K.

Unpolarized Raman spectra were collected at room temperature (300K) with a LabRAM HR 800 micro-Raman spectrometer with 1.96 and 2.41 eV argon laser incident light energy. The samples were focused by a x50 microscope objective. Power filters were used to avoid heating of the sample. Typical power densities on the surface sample were in the range of $0.25 \text{ mW}/\mu\text{m}^2$. The experimental results are presented in ref. 17 and Appendix A.

3. Results and discussion

3.1. Transmission Electron Microscopy: CNT and impurity observation

The as-produced SWNT powder (referred as “raw”) was purified using 2 different treatments: (i) a standard purification process that involves three main steps: air oxidation, acid reflux and annealing. The corresponding purified SWNT sample is referred as “sp”. (ii) An alternative halogen-based treatment that mainly consists in heating the SWNT powder under high chlorine partial pressure for 2 hours at 800°C, 950°C, or 1100°C [17], respectively assigned to “hp-800”, “hp-950”, “hp-1100”.

Fig. 1 shows typical TEM images of the raw SWNT sample and the purified sample by the standard purification procedure (sp) and one sample prepared by the chlorine-based process (hp-950) as a representative sample; hp-800 and hp-1100 showing quite similar aspects are not presented. As commonly observed, SWNTs are assembled into large bundles that could contain up to tens of tubes (Fig. 1a). Carbon impurities that are commonly included in arc-discharge as-produced SWNT samples are well visible in the raw SWNT sample (Fig. 1b). Metallic impurities are noticeable as dark spots surrounded by carbon layers or within amorphous carbon species (Fig. 1b). Accessibility of chemical reagents to metal-based

impurities is known to be highly reduced because of the well-known shielding effect by these carbon shells [9,13].

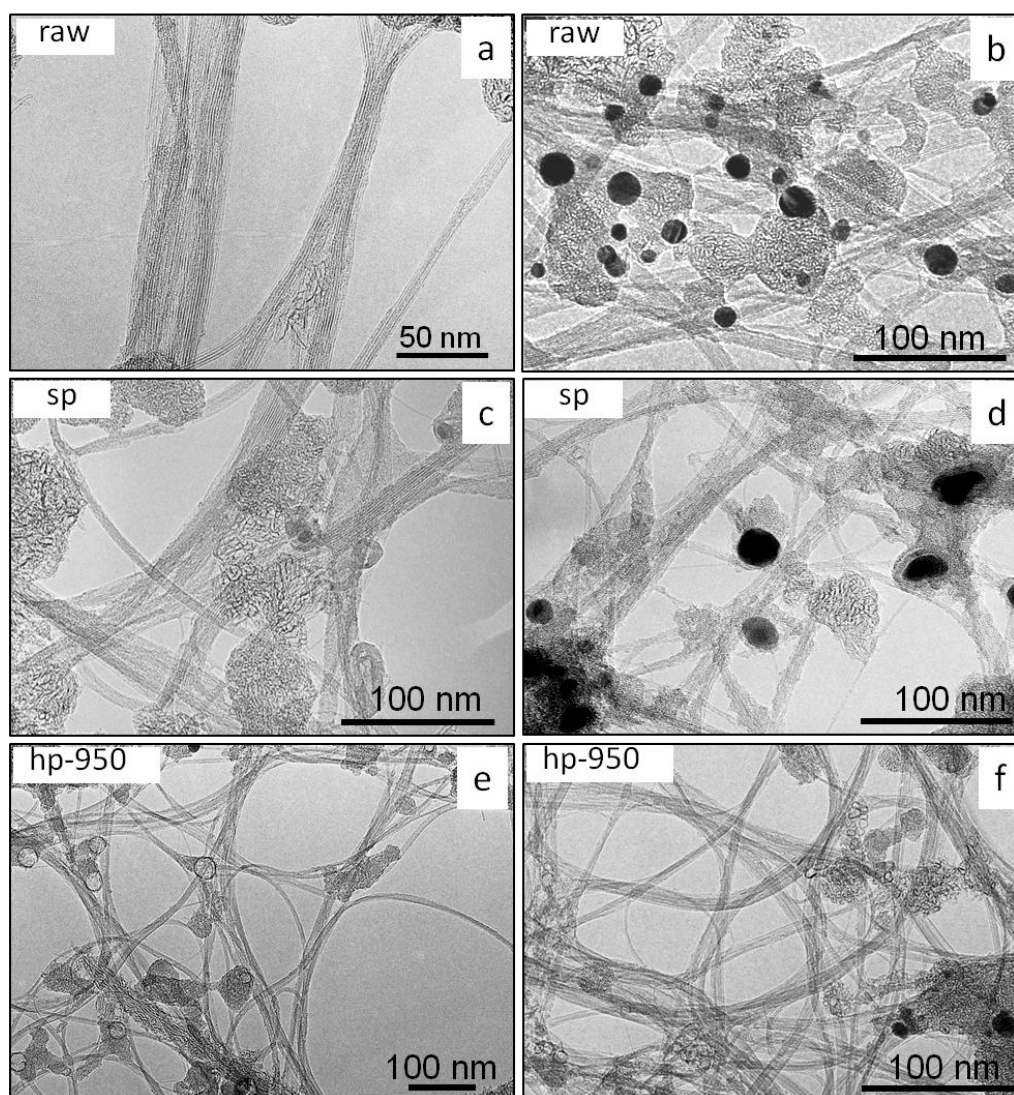


Fig. 1. TEM images of the raw sample, raw (a and b), a sample purified by a standard procedure, sp (c and d) and a sample purified by the chlorine-based process, hp-950 (e and f).

Chemical treatments which are usually strengthened in order to reach satisfactory metal removal yields are also responsible for damaging the CNT walls that have to be cured by a final annealing treatment. The developed chlorine-based process that allows to work at very high temperature (close to 1000°C) selectively favors the reactivity of the metal impurities.

Carbon impurities well visible in the raw sample are also noticeable after purification meaning that both applied treatments are not selective towards elimination of the carbon impurities (Fig 1c to 1f). The chlorine-based process advantageously preserves the structural quality of the purified SWNTs.¹⁷ In agreement with the observed decrease of I_D/I_G from Raman spectroscopy investigation (see Appendix 1), SWNT bundles appear undamaged and cleaned after the halogen-based purification (Fig. 1e and 1f), especially compared to the sample purified by the standard process (Fig. 1c and 1d). This decrease of I_D/I_G can be indeed attributed to the removal of thin carbon layers that cover the SWNT bundles at the raw state.²⁶ Another typical behavior observed after the purification using chlorine concerns the observation of numerous empty shells (Fig. 1e). Empty carbon shells were rarely observed in the sp sample.

TEM allows to determine the mean diameter of the metal-based particles ϕ_{TEM} as described in the experimental section. The results are reported in table 1. The size distribution is rather broad as shown by the images and the standard deviation. One can notice a decrease of the mean size of the remaining particles after the chlorine-based treatment, from 20 nm for the raw sample to 14 nm for the sample that was purified at 950°C under chlorine. The sample purified by the standard treatment differently behaves since the largest particles remain after purification in sp.

3.2. X-ray diffraction: investigation of Ni-based residues

Complementary to local TEM observations, XRD allows a global investigation of the samples. However, the low content and nano-meter size of the particles lead to weak diffraction peaks as shown in Fig. 2a. Diffraction pattern from the SWNTs are not recorded in our conditions; the more pronounced peak around 26° and those at 42° and 54° correspond to graphitic impurities (platelets and shells) commonly present in arc-discharge as-produced

SWNT samples. The major metal-based impurity, nickel is also detected. Ni(111), Ni(200) and Ni(220) (FCC structure) are well visible before purification (Fig. 2a). As usually observed for SWNT samples synthesized in our conditions; yttrium in too low content is not detected by XRD. As expected, the intensity of crystallized Ni diffraction peaks is significantly diminished after purification (Fig. 2b).

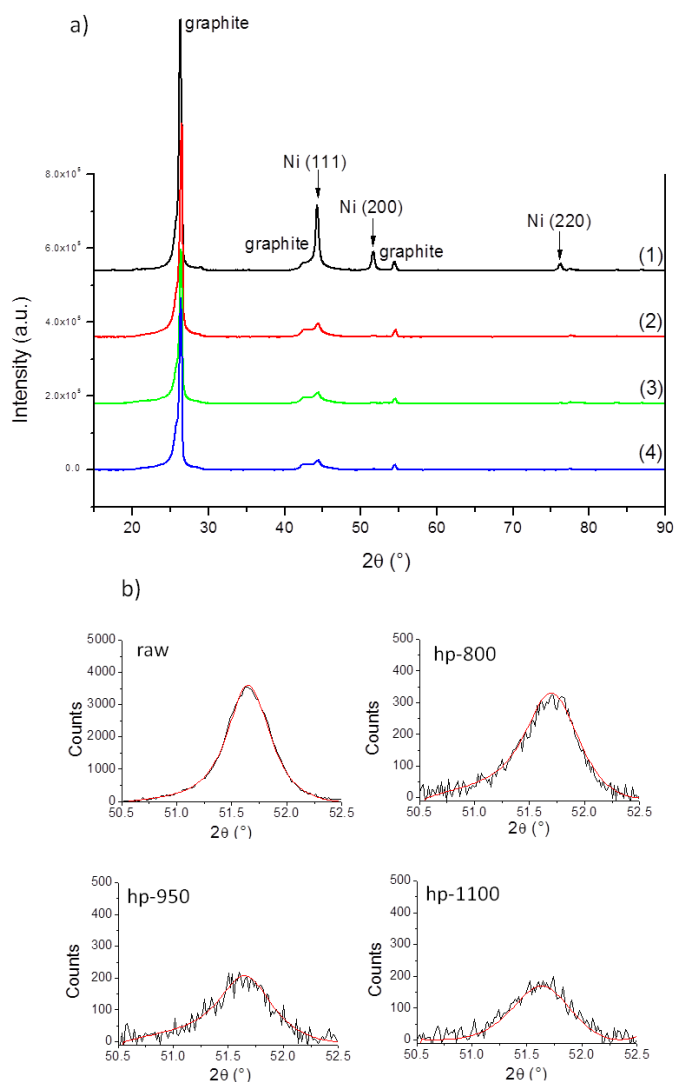


Fig. 2. Diffraction patterns of the raw and the purified samples. a): wide range and b): Ni(200) range (XRD data in black and curve resulting from the fit in red) of (1): raw, (2) hp-800, (3) hp-950, (4) hp-1100. Copper radiation $\text{CuK}\alpha$: $\lambda = 1.54056 \text{ \AA}$.

From the fitting of the Ni(002) diffraction peak by TOPAS (see Fig. 2b) and by means of the Scherrer formula, it was possible to evaluate a size of metallic catalyst nanoparticles. Indeed, as one uses the integral width of the peak to apply the Scherrer formula, the measured diameter is a mean diameter weighted by the volume distribution f_v [27]: $\phi^{XRD} = \int_0^\infty \phi f_v(\phi) d\phi$ with $f_v(\phi) = \frac{\phi^3 f(\phi)}{\int_0^\infty \phi^3 f(\phi) d\phi}$ where $f(\phi)$ is the normalized distribution function determined by TEM. The size determined by XRD is then $\phi^{XRD} = \frac{\int_0^\infty \phi^4 f(\phi) d\phi}{\int_0^\infty \phi^3 f(\phi) d\phi} = \frac{\langle \phi^4 \rangle}{\langle \phi^3 \rangle}$ whereas the size determined by TEM is $\phi^{TEM} = \int_0^\infty \phi f(\phi) d\phi$. As a matter of fact, the size determined from XRD has to be compared to the mean size measured by TEM and weighted by the volume of the particles: ϕ_{TEM}^v , which is given by $\phi_{TEM}^v = \frac{\langle \phi_{TEM}^4 \rangle}{\langle \phi_{TEM}^3 \rangle}$. The weight of the largest particles is then increased in ϕ_{TEM}^v with respect to ϕ_{TEM} . As a consequence, for all samples, ϕ_{TEM}^v is larger than ϕ_{TEM} (Table 1). In particular, one can notice that the largest shift is obtained for sp (41 nm versus 21 nm), in agreement with the large standard deviation of its size distribution (12 nm). Finally, as shown in table 1, ϕ_{TEM}^v is close to ϕ_{XRD}^v : taking into account the size distribution results in a good agreement between TEM and XRD for determining the size of the metal-based particles.

Table 1. Mean diameter of metal-based particles determined by TEM and XRD. σ_{TEM} is the standard deviation related to TEM measurements. The uncertainty of the mean values deduced from TEM corresponds to a level of confidence of 95%. The uncertainty of $\phi_{\text{XRD}}^{\text{v}}$ is provided by the fitting.

sample	ϕ_{TEM} (nm)	σ_{TEM} (nm)	$\phi_{\text{TEM}}^{\text{v}}$ (nm)	$\phi_{\text{XRD}}^{\text{v}}$ (nm)
raw	20 ± 1	7	27.0 ± 1.4	27 ± 1
sp	21 ± 3	12	41 ± 7	N.A.
hp-800	17.4 ± 1.3	6.5	24 ± 2	23 ± 5
hp-950	14 ± 2	6	20 ± 3	20 ± 7
hp-1100	N.A.	N.A.	N.A.	15 ± 4

Absolute quantitative analysis from XRD patterns for Ni impurities in the SWNT samples is not possible to perform because of the absence in the patterns of some phases such as amorphous carbon and nanotubes. However, relative crystallized Ni content of the purified samples with respect to that present in the raw one, RC_{Ni} , can be determined from the integration of a diffraction peak. This can be provided by the scale factor from the fitting by TOPAS from the Ni(200) peak (Fig. 1b). The results are given in table 2. Around 10 % of crystallized Ni remains in the Cl-treated samples, more precisely, it decreases from about 12 % to 8 % with increasing temperature treatment from 800°C to 1100°C.

Table 2. Ni content C_{Ni} and relative content RC_{Ni} determined from XRD, TGA and magnetic (MAG) investigations. C_{MxOy} is the remaining weight measured by TGA. RC_{Ni} of the purified sample is the weight % of remaining Ni with respect to its weight in the raw one. All contents are expressed in weight %.

sample	RC_{Ni} /XRD	C_{MxOy} (wt.%) / TGA	RC_{Ni} /TGA	C_{Ni} (wt.%) /TGA (equation 4)	C_{Ni} (wt.%) /MAG	C_{Ni}^0 (wt.%) /MAG	C_{Ni}^{2+}/C_{Ni}^0 MAG/ TGA
raw	100	10 ± 2	100	6 ± 1	4.8	4.8	0
sp	N.A.	5.4 ± 0.1	54	3.14 ± 0.06	2.7	2.7	0
hp-800	11.6	2.3 ± 0.2	23	1.3 ± 0.1	-	0.64	1.0
hp-950	8.4	3.0 ± 0.3	30	1.7 ± 0.2	-	0.53	2.3
hp-1100	7.6	2.2 ± 0.2	22	1.3 ± 0.1	-	0.46	1.8

3.3. Thermogravimetry Analysis: purification yields

TGA is commonly used as a quantitative technique to determine metal-based contents in CNT samples. It is estimated from the weight remaining at high temperature after burn off of the carbon species. Fig. 3 shows typical recorded thermograms for the raw and the purified samples. As typically observed the weight loss is more pronounced in the 450-650°C range due to combustion of carbon species, including amorphous carbon and carbon nanotubes. The less pronounced weight loss visible in the 700-800°C range is commonly attributed to

combustion of graphitized particles (platelets and shells) present in the SWNT sample. The weight of the samples is stabilized above 850°C (Fig. 3a, insert).

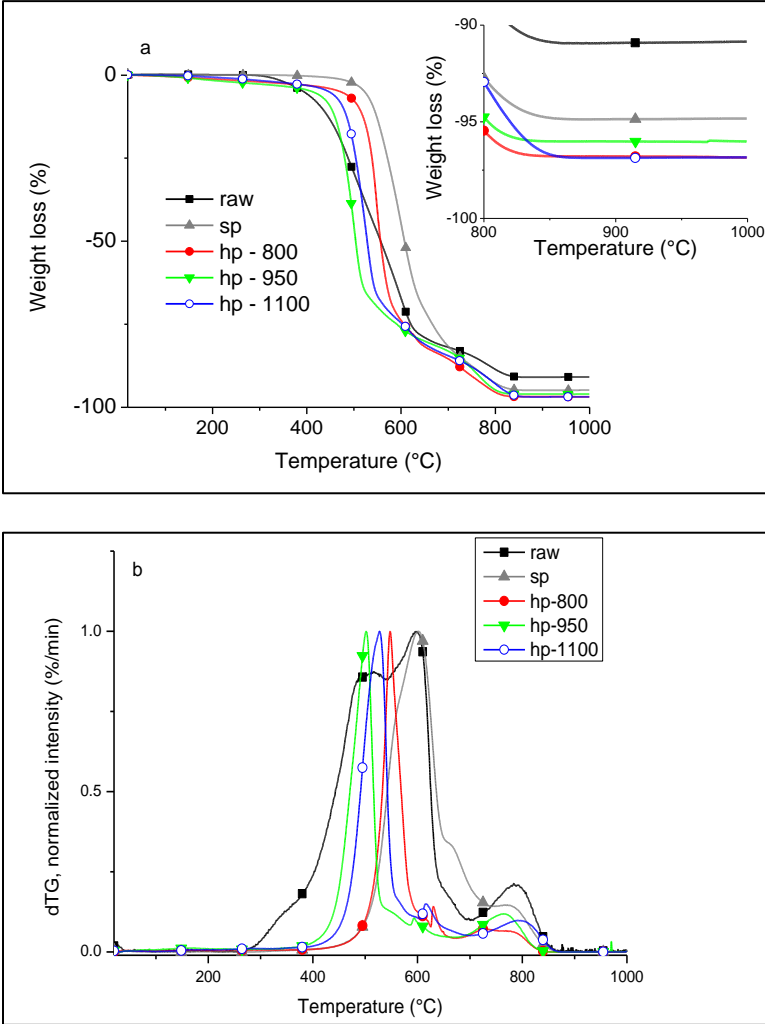


Fig. 3. Typical thermograms of a) the raw and the purified samples; black: raw; grey: sp ; red: hp-800; green: hp-950; blue: hp-1100;. Insert: magnified high temperature range; b) Derivative (dTG) representation of the weight losses.

The combustion temperature of the purified samples lies in the same temperature domain as that of the raw sample. However, the combustion domain appears narrower for the purified samples compared to that of the raw sample. The mean combustion temperature does not

follow a specific trend for the hp series: 550°C for hp-800, 500°C for hp-950 and 530°C for hp-1100 (Fig. 3b). sp shows also a narrow combustion temperature domain with a combustion temperature centered around 600°C ($\pm 40^\circ\text{C}$) which is only slightly up-shifted compare to that of the raw sample, around 550°C ($\pm 70^\circ\text{C}$) (Fig. 3b). The features of the thermograms are in agreement with TEM observations showing no significant modifications of the carbon species, whatever the applied treatment.

The residue weight, C_{MxOy} in % corresponds to the weight of the oxidized metals (NiO and Y_2O_3), m_{NiO} and $m_{\text{Y}_2\text{O}_3}$, divided by the initial total weight of the sample m_T .

$$C_{\text{MxOy}}(\%) = \frac{m_{\text{NiO}} + m_{\text{Y}_2\text{O}_3}}{m_T} \quad (1)$$

C_{MxOy} from the thermograms are reported in table 2. The relative Ni content in the purified samples with respect to the raw one, RC_{Ni} is deduced from C_{MxOy} assuming that the relative content Ni/Y is unchanged after the chemical treatments meaning that they do not selectively attack either Ni or Y. $\text{RC}_{\text{Ni}}/\text{TGA}$ is then simply given by the ratio of C_{MxOy} of the purified samples to that of the raw one. The values of the relative ratios deduced from TGA significantly deviate from those deduced from XRD: from a factor of 2 for hp-800 to a factor of 3 for hp-1100 (Table 2). MAG investigation will give an insight about this deviation in the following section. As TGA provides higher impurity content than XRD; it could be interesting to estimate the absolute content of Ni from the TGA results. Some conditions about the Ni/Y ratio and their respective oxidation state have then to be assumed: as commonly encountered, NiO and Y_2O_3 have been considered. As nickel is oxidized in the TGA chamber, formation of NiO from metal Ni leads to an increase of weight, IW, of:

$$\text{IW}_{\text{NiO}} = \frac{M_{\text{Ni}} + M_{\text{O}}}{M_{\text{Ni}}} = 1.2716 \quad (2)$$

And the gain of weight as Y is oxidized in Y_2O_3 is:

$$\text{IW}_{\text{Y}_2\text{O}_3} = \frac{2M_{\text{Y}} + 3M_{\text{O}}}{2M_{\text{Y}}} = 1.2700 \quad (3)$$

where M_x is the molar mass of the element x.

If we consider that Ni/Y ratio obtained in the as-produced and the treated samples is that used in the catalyst/graphite mixture for the synthesis; i.e. Ni/Y 4.2/1 at.% or $r = 2.83/1$ wt.%.

The corresponding mass ratio of the oxides, r_{ox} , is given by: $r_{ox} = r \frac{IW_{NiO}}{IW_{Y_2O_3}} = 2.83$

Content of nickel C_{Ni} in wt.% of the CNT samples can be determined from the residue weight, C_{MxOy} from the thermograms using Equation.4:

$$C_{Ni}(\%) = \frac{r_{ox}}{(r_{ox}+1)} \frac{C_{MxOy}(\%)}{IW_{NiO}} = \frac{C_{MxOy}(\%)}{1.72} \quad (4)$$

The results are reported in table 2. The Ni weight content of the raw sample is estimated at (6 ± 1) wt.%, it decreases roughly from a factor of 2 with the standard HCl treatment, and reaches values close to 1.5 wt.% with the Cl⁻ treatment. The metal removal yield of 75 % reported here is of the same range of standard purification processes involving a combination of acid reflux and oxidation treatments, used to purify several sources of CNTs [28]. Moreover, such treatment advantageously allows to avoid damaging the treated SWNTs.

3.4. Magnetic measurements: nature of the Ni species

In the case of magnetic impurities such as Ni, magnetic measurements which can be performed with a large amount of sample (several tens mg), is expected to provide a valid absolute content. Low field magnetization measurements performed as a function of temperature allow to characterize the different phases. Quantification can be extracted from high field measurements when the magnetic saturation is reached.

The field cooled (FC) and zero field cooled (ZFC) magnetization of the raw sample measured under 50 Oe is plotted in Fig. 4a.

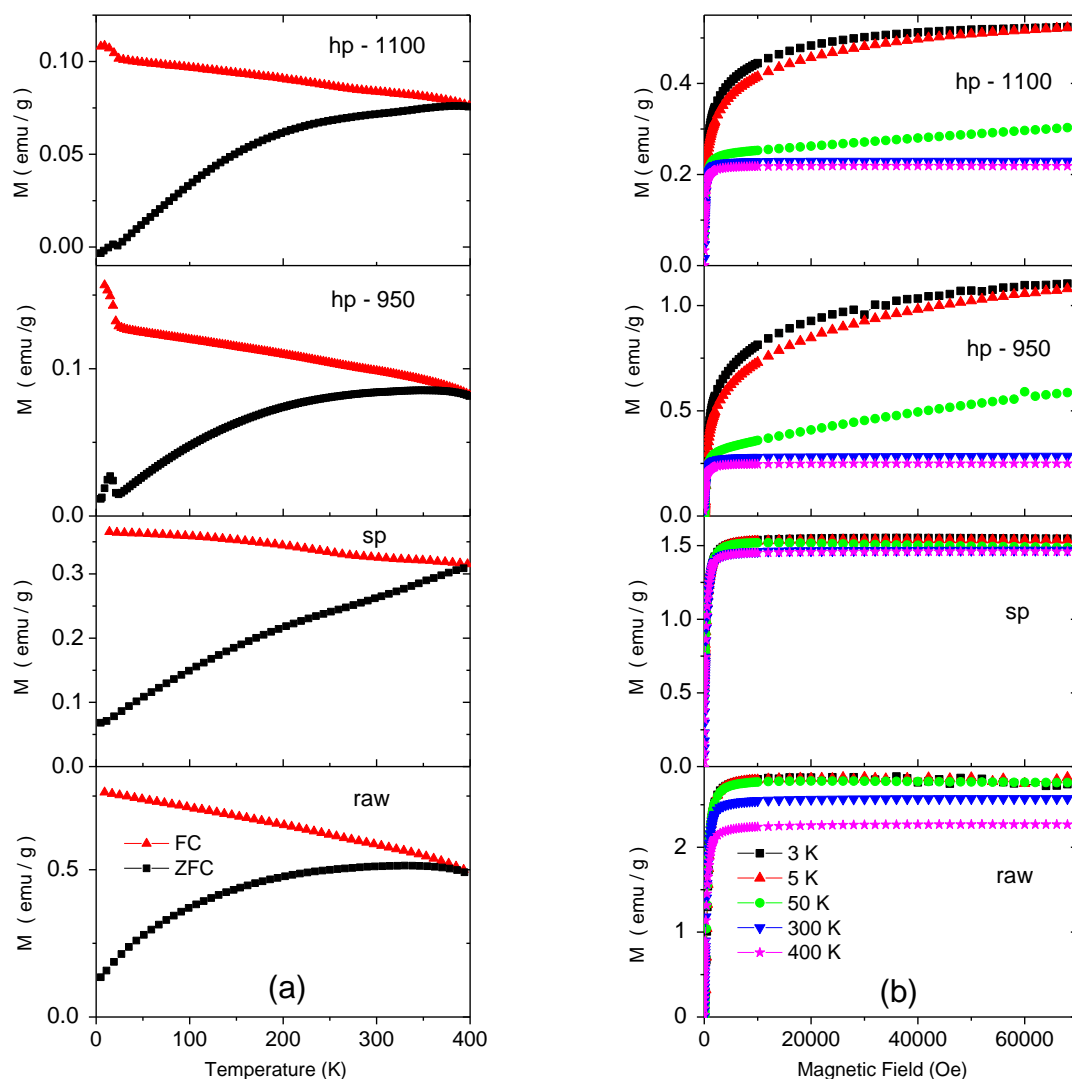


Fig. 4. (a) : Zero field cooled (ZFC) and field cooled (FC) magnetization as a function of temperature for the as-grown and purified samples measured under a field of 50 Oe. (b): field dependence of magnetization of as-grown and purified samples for several temperatures between 3K and 400K.

A large maximum of the ZFC temperature dependence is observed around 330K for the raw sample. No maximum is observed for the sample purified by the standard purification process (sp), indicating a shift of the blocking temperature towards higher temperature, above 400K. This feature can be correlated to the increase of the mean size of particles through the

standard purification process as observed by TEM (Table 1). Assuming the same origin of magnetic anisotropy, the blocking temperature is then proportional to the volume of the particle. No clear difference is observed between raw and hp samples in the ZFC curves above 20K. The FC curve of the raw sample shows a continuous decrease with increasing temperature from 5K to 400K without saturation at low temperature. It recovers the ZFC curve at the maximum temperature 400K. Qualitatively, the same features are observed for the purified samples, indicating in all cases a broad distribution of blocking temperatures, in agreement with the size distribution noticed by TEM.

More interestingly, the Cl-purified samples exhibit a peak in the ZFC curve and a sharp increase of the FC measurement below 20K. Fig. 5a focuses on this feature. This transition, missing in the raw and sp samples, indicates the presence of a magnetic compound produced by the Cl-purification process. This behavior is very close to the FC-ZFC curve of the NiCl₂ Graphite Intercalation Compound (NiCl₂-GIC) [29] attributed in that case to the occurrence of a 2D in-plane ferromagnetic order followed by an antiferromagnetic stack along the c-axis. Fig. 5b presents similar FC-ZFC measurements with an applied field of 500 Oe: both curves exhibit an increase of the signal with decreasing temperature, which is superposed to the features of the ordered phase mentioned above. This signal due to paramagnetic ions is attributed to isolated Ni²⁺ ions, readily attributed to NiCl₂ species. The latter could be located at the periphery of the remaining Ni particles or as intercalated species in between the layers of the carbon shells preventing them from oxidation by air. NiCl₂ is assumed to be an intermediate phase stabilized through the purification process.

Fig. 4b shows the field dependence of the magnetization for temperatures between 3K and 400K. The raw sample presents a saturation magnetization which slightly decreases with increasing temperature as expected for magnetic nanoparticles [30]. From the saturation magnetization measured at 3K, and assuming that the magnetization of the particles at low

temperature recovers the bulk value: $M_s^{\text{Ni}^0} = 58.6 \text{ emu/g}$, the weight percent of metallic Ni in the sample can be estimated around 4.8 wt.%. Considering the respective hypotheses required for TGA and MAG analysis, this value is in agreement with the result from TGA (6 ± 1) wt.%. The amount of Ni in the sp sample, estimated in the same way, is of about 2.7 wt.% which is close to the value obtained by TGA (3.1%) (Table 2). The evaluation from magnetic measurements depends on the value of the saturation magnetization of the nanoparticles which can be overestimated in the case of nanoparticles compared to that in the bulk state: some magnetic disorder or NiO thin layer at the particle surface can decrease the mean value of the saturation magnetization. For the Cl-treated samples, a huge increase of the signal is observed below 50K. It can be readily attributed to the contribution of Ni^{2+} , either in an ordered state (intercalated $\text{NiCl}_2\text{-GIC}$), as deduced from Fig. 5a or in a paramagnetic state (isolated spins), as shown in Fig. 5b.

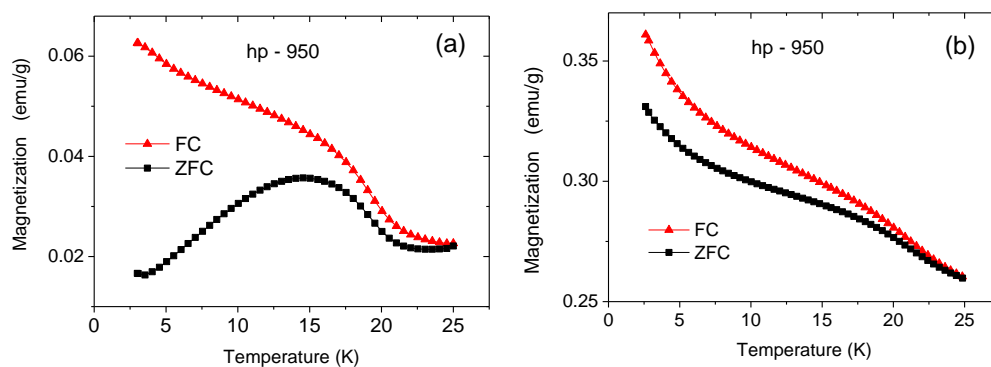


Fig. 5. Field cooled (FC) and zero field cooled (ZFC) magnetization of hp-950 in the temperature range 3K – 25K, for an applied field of 50 Oe (a), 500 Oe (b).

To evaluate the total amount of Ni in the Cl-purified samples, two contributions have then to be taken into account: the metallic Ni with a moment per atom of $0.616 \mu_B$ and the Ni^{2+} ions

with a moment of $2 \mu_B$ ($S = 1$) per atom. The contribution from paramagnetic Ni^{2+} being negligible at 400K, the weight percent of metallic Ni^0 is given by:

$$C_{\text{Ni}^0} = 100 \cdot \frac{M_s^{\text{hp}-\theta}(400 \text{ K})}{M_s^{\text{particles}}(400 \text{ K})} \quad (5)$$

where $M_s^{\text{particles}}(400 \text{ K})$ is the magnetization of the metallic nanoparticles at 400K and θ is the treatment temperature. $M_s^{\text{particles}}(400\text{K})$ can be evaluated from the temperature dependence of the saturation magnetization of the raw sample:

$$M_s^{\text{particles}}(400\text{K}) = M_s^{\text{raw}}(400\text{K}) \frac{M_s^{\text{Ni}^0}}{M_s^{\text{raw}}(3\text{K})} \quad (6)$$

The Ni^0 content deduced from MAG is reported in table 2. It decreases from roughly a factor of 10 with the halogen treatment, in agreement with the relative content deduced from XRD. Ni^0 content also slightly decreases with the temperature treatment as deduced from XRD.

The amount of Ni^{2+} can then be deduced from the high field, low temperature magnetization by subtracting the contribution of metallic Ni^0 as:

$$C_{\text{Ni}^{2+}} = \frac{100 \cdot M_s^{\text{hp}-\theta}(3\text{K}, 7\text{T}) - C_{\text{Ni}^0} \cdot M_s^{\text{Ni}^0}}{M_s^{\text{Ni}^{2+}}} \quad (7)$$

with $M_s^{\text{Ni}^0} = 58.6 \text{ emu/g}$ and $M_s^{\text{Ni}^{2+}} = 187 \text{ emu/g}$

Equation (7) assumes that the magnetization reaches saturation at 3K for 70 kOe. This is valid for both the ordered state [29] and paramagnetic spins (a $S = 1$ spin reaches 95% of its saturation magnetization at 3K under 70 kOe).

The total relative content of Ni determined by MAG is then the sum of the relative content of Ni^0 and Ni^{2+} , $(C_{\text{Ni}^0} + C_{\text{Ni}^{2+}})/C_{\text{Ni}}(\text{raw})$, reported in Fig. 6.

Fig. 6 gathers the relative Ni content with respect to raw sample, determined by the different used techniques. For the sp treatment, a good agreement is observed between magnetic and TGA results, which asserts the evaluation. In the case of hp-treatments, the relative content of

crystalline Ni (provided by XRD) is close to the relative content of Ni in ferromagnetic particles as determined by MAG. Despite the contribution of Ni^{2+} , a huge discrepancy remains between the total amount of Ni element determined by TGA and the evaluation from MAG, and this discrepancy is enhanced by the temperature treatment.

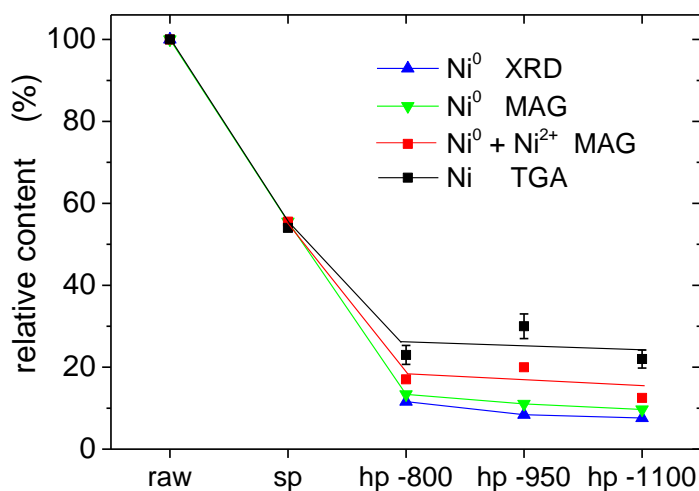


Fig. 6. Relative content of residual nickel in the treated samples with respect to raw sample determined by TGA, X-ray diffraction (XRD), and magnetic measurements (MAG).

Low temperature measurements have revealed the presence of Ni^{2+} , paramagnetic above 20K, whose signal is superimposed to that of ferromagnetic grains. As a consequence, the paramagnetic phase can be characterized at high temperature only under high field for which the signal coming from the grains is saturated. Fig. 7 shows the temperature dependence of magnetization of hp-1100 under 50 kOe. In case of ferro- or paramagnetic signals, one expects an increase of magnetization with decreasing temperature. On the contrary, with decreasing temperature, a surprising decrease of the signal is observed below 260K followed by an upturn below 170K.

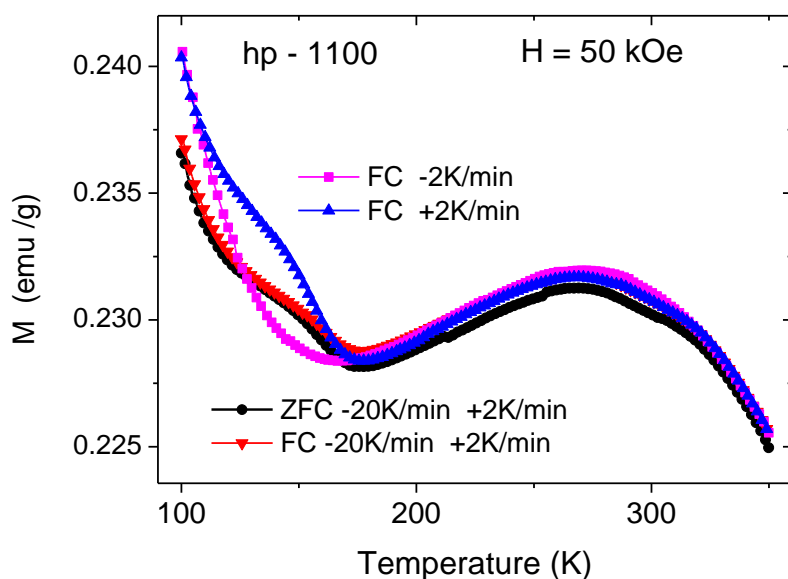


Fig. 7. Field and temperature hysteresis of the temperature dependence of the magnetization of hp – 1100 measured under 50 kOe. The field cooling effect correspond to the ZFC (black line) and FC (red line) curves measured with increasing temperature at a rate of +2 K/min after a cooling at -20K / min. The temperature hysteresis is measured under the same applied field with decreasing and increasing temperature at a rate of – 2 K/min or +2 K/min.

The field cooling behavior has been checked with ZFC and FC measurements. The sample is cooled under zero field (ZFC) or applied field (FC) at a rate of -20 K/min, and the measurements are performed in both cases with increasing temperature at a rate of +2 K/min. No irreversibility is observed between both measurements. On the contrary, temperature measurements performed with decreasing and increasing temperature (FC -2 K/min and FC +2 K/min) exhibit some hysteresis below 170K. Such behavior is often observed in high spin – low spin crossover [31]. Spin crossover appears generally when the ion is strained, the coordination sphere of the low spin being smaller than in a high spin state. In case of Ni^{2+} , it corresponds to a transition between the paramagnetic state with $S = 1$, and the diamagnetic

one, $S = 0$. In that case, the total contribution of Ni^{2+} could be estimated only from the temperature dependence of the paramagnetic signal above the spin crossover, that is above 300K. This could be possible if there were no other contribution to the magnetic signal. In the present case, because of the contribution of the Ni grains, no reliable quantification from magnetic measurements can be performed; the evaluation of the Ni content from MAG presented in Fig. 6 is intrinsically incomplete. The large discrepancy between XRD and TGA quantifications is then due to Ni^{2+} either in high spin ($S = 1$) or low spin ($S = 0$) state.

As a consequence, for the chlorine-based treatment, only TGA provides an absolute reliable evaluation of the Ni content. The hp treatment provides the low Ni content, but no effect of the temperature used for the treatment is observed on the nickel removal efficiency. In fact, Fig. 6 shows that the discrepancy between TGA and MAG evaluation increases with temperature. As it is attributed to the contribution of Ni^{2+} with $S = 0$, increasing the temperature treatment under chlorine favors the reaction of Ni with Cl, and then decreases the metallic Ni^0 content, as observed by XRD and MAG, but does not lead to improve the purification process since Ni^{2+} remains in the samples. The ratio $\text{Ni}^{2+}/\text{Ni}^0$ of the hp samples can be estimated by combining TAG and MAG results:

$$\frac{C_{\text{Ni}^{2+}}}{C_{\text{Ni}^0}} = \frac{C_{\text{Ni}}(\text{TGA})}{C_{\text{Ni}^0}(\text{MAG})} - 1 \quad (8)$$

$\text{Ni}^{2+}/\text{Ni}^0$ ratio is reported in table 2, it increases from 1 to roughly 2 with increasing temperature treatment from 800°C to 950 – 1100 °C. A limitation of the efficiency of the developed Cl-based treatment on the arc-discharged as-produced samples is here evidenced. This effect is certainly enhanced by a high content of carbon multi-layer shells and graphitic particles in these SWNT samples compared to those from HiPco CVD synthesis for which such Cl-based treatment was shown to be improved with temperature [32].

Fig. 8 focuses on the low field hysteresis loop measured at 400K of the raw, sp and hp-950 samples. One can notice that a very similar shape is observed for sp and raw, with a slightly more open loop for sp.

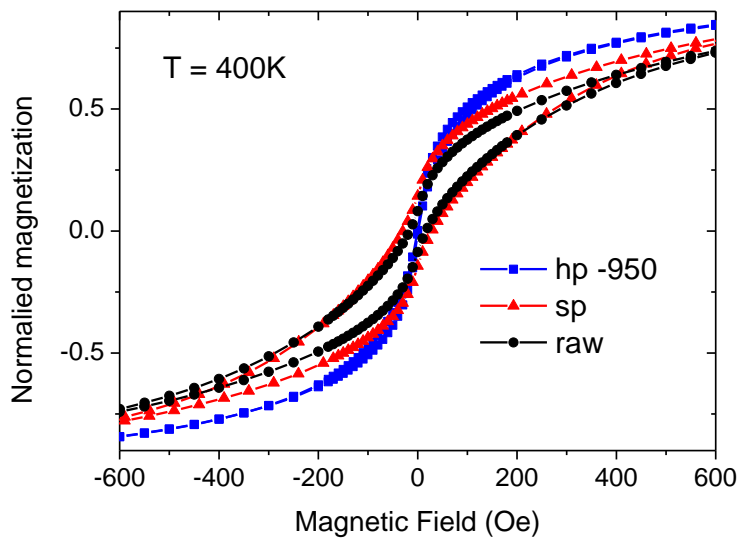


Fig. 8. Field dependence of the normalized magnetization for $H = 2$ kOe, at $T = 400$ K of the raw and treated samples.

On the contrary, the hp hysteric loop appears almost reversible. These features have to be correlated to TEM, XRD and FC-ZFC measurements. All observations are in agreement with the fact that the sp treatment does not attack the largest particles, which remain intact, whereas they are easily removed by the hp treatment. This selectivity in treatments reveals a chemical differentiation of the particles associated to their size. It is clear from TEM that some particles are well protected by carbon shells, if not, it is reasonable to assume that some NiO oxide is present at the surface of the particles. It is expected that the sp process preferentially attack the NiO particles and Ni non-protected by carbon shells. On the contrary, the hp treatment removes preferentially the particles inside the carbon shell whereas the

reaction with NiO is less favorable. In that case, both treatments would be complementary and should be combined to reach a better quantitative efficiency.

4. Conclusion

Quantitative analysis of metal-based residues in SWNT samples after chemical purification is an open and tricky question. In this work, we have investigated the commonly used characterization techniques combined with magnetization measurements. This latter allows to determine the exact state of the impurities that is of importance to know the chemical mechanisms involved in the purification treatments. Based on two different purification procedures, the results are discussed regarding the limitations of both the characterization techniques and the chemical purification weaknesses. The Cl-gas phase treatment is found to be the most efficient in terms of Ni-impurity content, moreover, it preserves the quality of the nanotubes. We show that this treatment modifies the oxidation state of the impurities, and leaves some NiCl₂ species which are either paramagnetic or intercalated into graphitic carbon forming an ordered magnetic phase. This feature complicates the quantitative analysis. In the paramagnetic phase, Ni²⁺ can be in the high spin state ($S = 1$) or in the low spin state ($S = 0$, diamagnetic) and is then ruled out for the magnetic measurements. Moreover, whatever the temperature of the Cl-treatment, the Ni weight percent is found to be limited at about 1.5 wt.%. Increasing the temperature allows to transform Ni in Ni²⁺, but do not allow to improve removal of the produced Ni species which remain trapped in the sample. Such byproduct formation occurring during a purification treatment is rarely reported, but has nevertheless to be taken into account in the choice of the purification technique, whose criterions depend on the application of the CNTs.

Acknowledgments. The authors thank Jean-François Marêché for his technical help for the chemical treatments. The authors would like to thank Lionel Aranda for his help for TGA experiments and Pascal Franchetti for his valuable assistance for Raman spectroscopy.

Appendix

Raman spectroscopy was systematically performed before and after each chemical treatment to follow the evolution of CNT crystalline properties throughout the whole purification steps. Typical SWNT Raman spectra present three main bands: (i) Radial Breathing Modes (RBM) appearing from 100 up to 500 cm^{-1} are strongly dependent on the CNT diameter since they correspond to the atomic vibration of the C atoms in the radial direction [33]; (ii) the D band, noticeable around 1345 cm^{-1} , can be activated either by the presence of defects in CNT walls or by the presence of amorphous carbon (for more details see refs 10 and 33 and references therein). (iii) the graphite-like G band due to the tangential phonon modes of a graphene sheet is present between 1570 and 1593 cm^{-1} . In SWNTs it is split in two peaks G^- and G^+ around 1556 and 1592 cm^{-1} , respectively.

The ratio between the intensity of the D and G peaks (I_D/I_G) is widely used to state the structural quality of CNTs [34]. Typically, I_D/I_G (I_D/I_{G^+} for SWNTs) < 1 indicates a low concentration of defects/amorphous carbon that is the fingerprint of good crystalline quality. In table A1 and ref. 17 we present the experimental data obtained by Raman spectroscopy with both $E_1=1.96$ and $E_2=2.41$ eV laser energies. Firstly, we can observe that the average I_D/I_{G^+} ratio taken from Raman spectra on several samples with both excitation energies decrease after the purification treatment. This finding indicates that the adopted purification process preserves the crystalline quality of the pristine nanotubes or even improves it thanks to an annealing effect intrinsic to the cited chemical treatment.

Secondly, the diameters of those SWNT resonating at E_1 and/or E_2 were estimated through the relation $\omega_{\text{RBM}}=A/d_t + B$, where ω_{RBM} represents the RBM peak frequencies in Raman spectra. We assumed $A= 234 \text{ cm}^{-1} \text{ nm}$ and $B= 10 \text{ cm}^{-1}$ as the value generally accepted for SWNT bundles with average diameter near about 1.5 nm [35]. The calculated diameters are

shown in table A1. As main feature, we note a tube diameter distribution centered in the interval 1.3-1.7 nm, almost purification independent.

Finally, the electronic properties of the resonating nanotubes as derived from Kataura's plot are reported in table A1 [36,37]. Gray and brown colors represent semiconducting and metallic nanotubes respectively. As expected, the majority of the resonating tubes are semiconducting since only about one third of the analyzed samples can be metallic. Limited to the present statistics, data shown in table A1 suggest that used chemical purification treatment is not selective respect to SWNT electric properties.

Table A1. I_D/I_{G+} average ratio and tube diameter as determined by Raman spectroscopy (see text for details). "R" and "G" states for red ($E_1=1.96$ eV) and green ($E_2=2.41$ eV) lasers, respectively. The grey and brown background colors indicate semiconducting and metallic electronic properties as deduced by using the Kataura's plot.

sample	$\langle I_D/I_{G+} \rangle$	$\langle I_D/I_{G+} \rangle$	diameters (nm)									
	(R)	(G)	1.3	1.4	1.5	1.6	1.7	1.8				
raw	1.1	0.5	R	G	G	R	G		G	R	G	
hp-950	0.9	0.18	R	G	G	R	G	R	G	R	G	G
hp-1100	0.9	0.11	R	G	G	R	G		G			

References

- [1] P. M. Ajayan, *Chem. Rev.* **99**, 1787 (1999).
- [2] H. Dai, *Acc. Chem. Res.* **35**, 1035 (2002).
- [3] I. W. Chiang, B. E. Brinson, R. E. Smalley, J. L. Margrave, and R. H. Hauge. *J. Phys. Chem. B* **105**, 1157 (2001).
- [4] R. Brukh, O. Sae-Khow, S. Mitra, *Chem. Phys. Lett.* **459**, 149 (2008).
- [5] A. V. Ellis, and B. Ingham, *J. Mag. Mag. Mats.* **302**, 378 (2006).
- [6] J. P. Salvetat, T. Fehér, C. L'Huillier, F. Beuneu, and L. Forró, *Phys. Rev. B* **72**, 075440 (2005).
- [7] M. Pumera, and Y. Miyahara, *Nanoscale* **1**, 260 (2009).
- [8] H. G. Cho, S. W. Kim, H. J. Lim, C. H. Yun, H. S. Lee, and C. R. Park, *Carbon* **47**, 3544 (2009).
- [9] G. Charron, S. Mazerat, M. Erdogan, A. Gloter, A. Filoramo, J. Cambedouzou, P. Launois, E. Rivière, W. Wernsdorfer, J.-P. Bourgoin, Talal Mallah, *New J. Chem.* **33**,1211 (2009).
- [10] A. C. Dillon, T. Gennett, K. M. Jones, J. L. Alleman, P. A. Parilla, and M. J. Heben, *Adv. Mater.* **11**, 1354 (1999).
- [11] B. Yu, P. X. Hou, F. Li, B. Liu, C. Liu, and H. M. Cheng, *Carbon* **48**, 2941 (2010).
- [12] M. T. Martinez, M. A. Callejas, A. M. Benito, M. Cochet, T. Seeger, A. Anson, J. Schreiber, C. Gordon, C. Marhic, O. Chauvet, J. L. G. Fierro, W. K. Maser, *Carbon* **41**, 2247 (2003).
- [13] B. Vigolo, C. Hérold, J.-F. Marêché, J. Ghanbaja, M. Gulas, F. Le Normand, R. Almairac, L. Alvarez, and J.-L. Bantignies, *Carbon* **48**, 949 (2010).
- [14] J. L. Zimmerman, R. Kelley Bradley, C. B. Huffman, R. H. Hauge, and J. L. Margrave, *Chem. Mat.* **12**, 1361 (2000).

- [15] Y. Q. Xu, H. Peng, R. H. Hauge, and R. E. Smalley. *Nanolett.* **5**, 163 (2005).
- [16] G. Mercier, J. Gleize, J. Ghanbaja, J.-F. Marêché, and B. Vigolo, *J. Phys. Chem. C* **117**, 8522 (2013).
- [17] G. Mercier, C. Hérold, J.-F. Marêché, S. Cahen, J. Gleize, J. Ghanbaja, G. Lamura, C. Bellouard, and B. Vigolo, *New J. Chem.* **37**, 790 (2013).
- [18] E. L. K. Chng, H. L. Poh, Z. Soferb, and M. Pumera, *Phys. Chem. Chem. Phys.* **15**, 5615 (2013).
- [19] T. Kolodiazhnyi, and M. Pumera, *Small* **4**, 1476 (2008).
- [20] E. Pellicer, A. B. González-Guerrero, J. Nogués, L. M. Lechuga, and E. Mendoza, *Carbon* **47**, 758 (2009).
- [21] B. Ballesteros, G. Tobias, L. Shao, E. Pellicer, J. Nogués, E. Mendoza, and M. Green, *Small* **4**, 1501 (2008).
- [22] B. Pacakova, Z. Kominkova, J. Vejpravova, A. Mantlikova, and M. Kalbac, *J. Mat. Sci.* **50**, 2544 (2015).
- [23] B. Bittova, J. Vejpravova, M. Kalbac, S. Burianova, A. Mantlikova, S. Danis, and S. Doyle, *J. Phys. Chem. C* **115**, 17303 (2011).
- [24] B. Bittova, M. Kalbac, S. Kubickova, A. Mantlikova, S. Mangold, and J. Vejpravova, *Phys. Chem. Chem. Phys.* **15**, 5992 (2013).
- [25] F. Chen, Y. Xue, V. G. Hadjiev, C. W. Chu, P. Nikolaev, and S. Arepalli, *Appl. Phys. Lett.* **83**, 4601 (2003).
- [26] S. Osswald, E. Flahaut, H. Ye, and Y. Gogotsi, *Chem. Phys. Lett.* **402**, 422 (2005).
- [27] G. A. Martin, *Revue Phys. Appl.* **16**, 181 (1981).
- [28] A. B. Makama, A. Salmiaton, N. Abdullah, Thomas S. Y. Choong, E. B. Saion. *Separation Sci. and Technol.* **49**, 2797 (2014).
- [29] I. S. Susuki, M. Susuki. *J. Phys.: Condens. Matter.* **10**, 5399 (1998).

- [30] J. L. Dormann, D. Fiorani, E. Tronc. *Adv. Chem. Phys.* **98**, 283 (1997).
- [31] S. Brooker. *Chem. Soc. Rev.* **44**, 2880 (2015).
- [32] E. Remy, S. Cahen, B. Malaman, J. Ghanbaja, C. Bellouard, G. Medjahdi, A. Desforages, S. Fontana, J. Gleize, B. Vigolo, C. Hérold. *Carbon* **93**, 933 (2015).
- [33] G. Lamura, A. Andreone, Y. Yang, P. Barbara, B. Vigolo, C. Hérold, J.-F. Marêché, P. Lagrange, M. Cazayous, A. Sacuto, M. Passacantando, F. Bussolotti, M. Nardone. *J. Phys. Chem. C* **111**, 15154 (2007).
- [34] P. Delhaes, M. Couzi, M. Trinquocoste, J. Dentzer, H. Hamidou, C. A. Vix-Guterl. *Carbon* **44**, 3005 (2006).
- [35] A. Jorio, M. A. Pimenta, A. G. Souza Filho, R. Saito, G. Dresselhaus, M. S. Dresselhaus. *New. J. Phys.* **5**, 139.1 (2003).
- [36] H. Kataura, Y. Kumazawa, Y. Maniwa, I. Umezu, S. Suzuki, Y. Ohtsuka, Y. Achiba. *Synth. Met.* **103**, 2555 (1999).
- [37] A. Jorio, A. G. Souza Filho, G. Dresselhaus, M. S. Dresselhaus, A. K. Swan, M. S. Ünlü, B. B. Goldberg, M. A. Pimenta, J. H. Hafner, C. M. Lieber, R. Saito. *Phys. Rev. B* **65**, 155412.1, (2002).